Current Biology 19, 1861–1868, November 17, 2009 ©2009 Elsevier Ltd All rights reserved DOI 10.1016/j.cub.2009.09.063

Report

The Fission Yeast TACC Protein Mia1p Stabilizes Microtubule Arrays by Length-Independent Crosslinking

Rahul Thadani,[1,2] Yuen Chyao Ling,[1,2] and Snezhana Oliferenko[1,*]
[1]Temasek Life Sciences Laboratory, 1 Research Link, Singapore 117604, Singapore

Summary

Microtubule (MT) arrays are mechanistic effectors of polarity specification and cell division. Linear bundles in which MTs are bridged laterally [1, 2] are dynamically assembled in systems ranging from differentiated metazoan cells to fungi in a process that remains poorly understood. Often, bundled MTs slide with respect to each other via molecular motors [3, 4]. In interphase cells of the fission yeast *Schizosaccharomyces pombe*, MT nucleation frequently occurs at preexisting arrays [5, 6]. As the nascent MT lengthens, stable antiparallel MT overlaps are thought to form through competition between motion of the minus-end-directed kinesin Klp2p [4] and braking force exerted by the accumulating lateral crosslinker Ase1p [7–9]. Here we show that Mia1p/Alp7p, a transforming acidic coiled-coil (TACC) protein [10, 11], functions as a length-independent MT crosslinker. In cells lacking Mia1p MT-bundling activity, linear arrays frequently disassemble, accompanied by a marked increase in Ase1p off rate and erratic motion of sliding MTs. We propose that the combined action of lateral length-dependent (Ase1p) and terminal length-independent (Mia1p) crosslinkers is crucial for robust assembly and stability of linear MT arrays. Such use of qualitatively distinct crosslinking mechanisms in tandem may point to a general design principle in the engineering of stable cytoskeletal assemblies.

Results and Discussion

In interphase cells, Mia1p-3GFP localized as dots along mCherry-α-tubulin-labeled microtubules (MTs) and was enriched at MT overlaps but also seen at MT plus ends (Figure 1A). Notably, Mia1p-3GFP fluorescence intensity peaked at edges of MT overlaps (Figures 1B and 1C) and only weakly correlated with overlap length ($r = 0.38$, $p < 0.01$, $n = 56$; see Figure S1A available online). Consistent with enrichment at MT minus ends, Mia1p partially colocalized with the γ-tubulin accessory factor Mto1p-mCherry (Figure 1D). We confirmed the MT plus-end localization of Mia1p by coimaging Mia1p-3GFP and the plus-end marker Tip1p-mCherry (Figure 1E).

Purified recombinant MBP-Mia1p (Figure S1B) cosedimented with taxol-stabilized MTs (Figure 1F) with a dissociation constant K_D of 0.88 μM (Figure 1G; Figure S1C). MBP-Mia1p also directly interacted with tubulin heterodimers (Figure S1D). When mixed with rhodamine-labeled MTs, purified tag-free Mia1p induced rapid appearance of MT bundles (Figure 1H). Transmission electron microscopy showed MTs tightly aligned in regions of linear bundling, leading to frequent appearance of fan-shaped structures (Figure 1I). We examined the orientation of MTs in bundles with polarity-marked MTs and found that 68% of bundles were antiparallel, whereas the remaining 32% were parallel (Figure 1J, $n = 59$ bundles). Recombinant His_6-Mia1p-GFP localized to MT overlaps when mixed with rhodamine-labeled MTs (Figures 1K and 1L). We thus concluded that in vitro, Mia1p promiscuously binds MTs to induce formation of linear bundles.

We then employed deletion mutagenesis to generate an Mia1p mutant specifically deficient in MT bundling. Based on a multiple alignment of transforming acidic coiled-coil (TACC) proteins, we detected three conservation peaks at amino acids 151–300, 301–387, and 388–474 of Mia1p (Figure S2A), indicating the boundaries of putative functional domains. Secondary structure prediction algorithms suggested that the region downstream of residue 150 was rich in α helices and contained coiled coils ([12], Figures S2A and S2B).

Ectopically expressed N-terminal (Mia1p-1-300-GFP) and C-terminal (Mia1p-301-474-GFP) deletion mutants of Mia1p both showed aberrant distribution compared to full-length Mia1p, which localized to MTs and the spindle pole bodies (SPBs) in wild-type (Figure 2A) and *mia1*Δ (Figure S3A) cells. Because Mia1p-1-300-GFP does not contain a nuclear export sequence [13], it was restricted to the nucleus, where it localized to spindle MTs (Figure 2A). However, this construct could bind cytoplasmic MTs when we disrupted the nuclear envelope with a temperature-sensitive RanGEF mutation [14] (Figure S3B). This suggested that Mia1p-1-300-GFP contained the de facto MT-binding activity. Conversely, Mia1p-301-474-GFP localized mainly to the SPBs and very weakly as dots on MTs but was depleted from MT overlaps (Figure 2A; Figure S3A). MBP-Mia1p-1-300 cosedimented with MTs in a spin-down assay, whereas MBP-Mia1p-301-474 did not (Figure 2B). Within the first 300 amino acids lies a conserved α-helical region spanning amino acids 151–300 (predicted to form a coiled coil at residues 244–256). A mutant protein lacking this region, MBP-Mia1p-Δ151-300, retained the ability to bind to MTs (Figure 2B). Strikingly, Mia1p-Δ151-300 failed to bundle MTs in vitro, unlike Mia1p and Mia1p-1-300 (Figure 2C). We concluded that MT-binding activity centered on Mia1p-1-300 and that the α-helical-rich region spanning residues 151–300 was crucial for MT bundling. The GFP-tagged bundling mutant Mia1p-Δ151-300-GFP, expressed under the native promoter, was abundant (Figure S3C) and localized to the SPB but was depleted from MTs (Figure 2D).

Our results thus far suggested that Mia1p might function as an MT crosslinker. Therefore, we examined interphase MT dynamics in *mia1Δ151-300* cells, where Mia1p could not bundle MTs. We observed comparable MT growth (2 ± 0.2 μm min^{-1} versus 2.3 ± 0.3 μm min^{-1}) and depolymerization (7.4 ± 0.02 μm min^{-1} versus 7.1 ± 0.02 μm min^{-1}) rates in wild-type and *mia1Δ151-300* cells. Both strains exhibited similar numbers of MT plus ends, labeled by an EB1 protein, Mal3p-GFP (11 ± 2 versus 12 ± 1.8, $n = 20$ cells), and comparable probabilities of survival of newly nucleated MTs (0.91, $n = 185$ MTs versus 0.84, $n = 200$ MTs). Concordantly, interaction of the MT-stabilizing protein Alp14p [15] with Mia1p (Figures S3D and S3E) and Klp2p recruitment to MTs (Figure S3F)

*Correspondence: snejana@tll.org.sg
[2]These authors contributed equally to this work

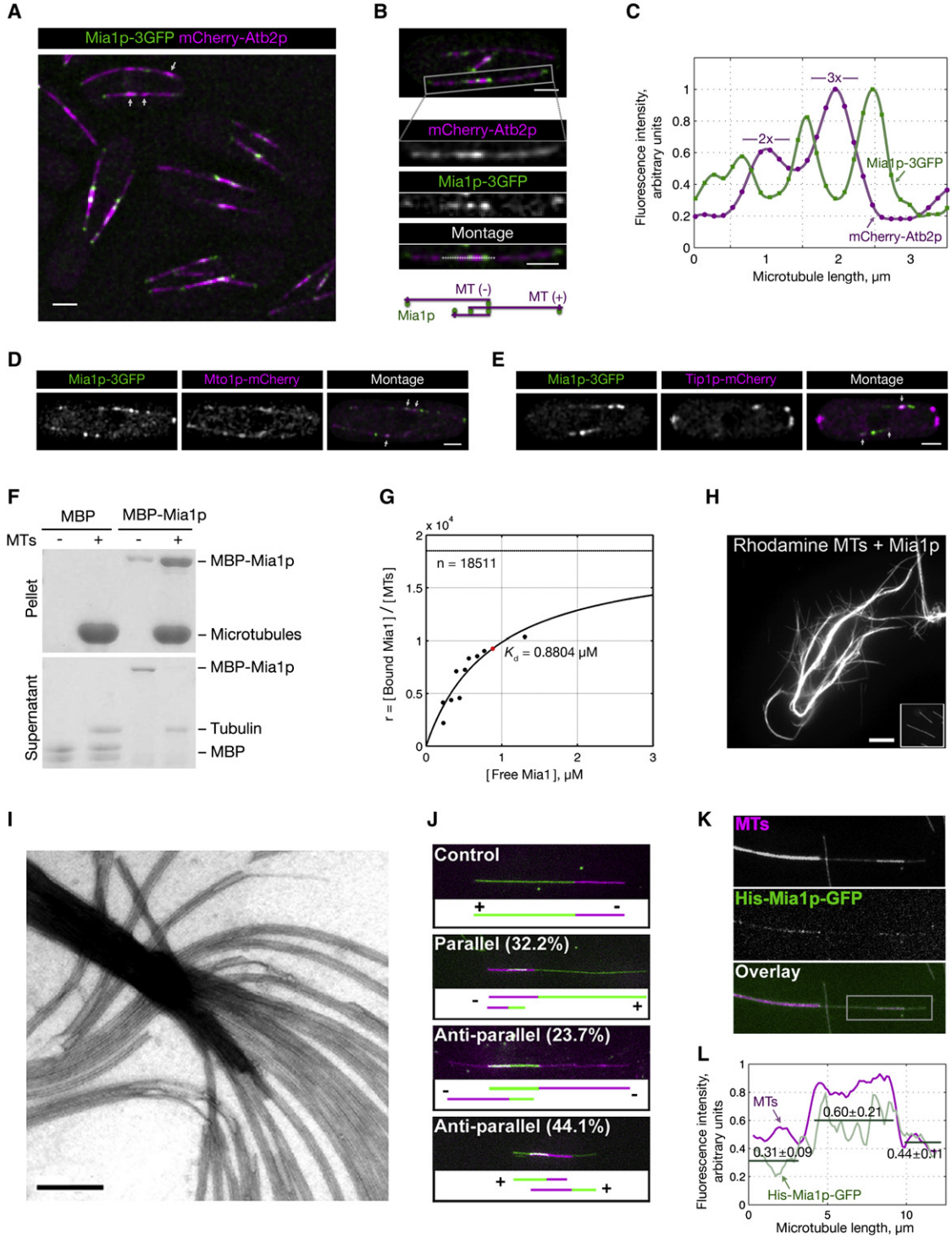

Figure 1. Mia1p Flanks Microtubule Overlaps In Vivo and Bundles Microtubules In Vitro

(A) Mia1p-3GFP (green) localizes along mCherry-α-tubulin-labeled microtubules (MTs) (magenta). Arrows mark a medial region of overlap and a nascent bundle at the periphery. Shown is a deconvolved maximum-intensity reconstruction. Scale bar represents 2 μm.

(B) Mia1p-3GFP flanks a medial MT overlap. Magnified: single confocal plane with a schematic interpretation (bottom). Scale bar represents 2 μm.

(C) Fluorescence intensity profiles of Mia1p-3GFP and mCherry-Atb2p along the dotted line shown in (B).

(D and E) Mia1p-3GFP partially colocalizes with Mto1p-mCherry (D) and Tip1p-mCherry (E). Shown is a maximum-intensity reconstruction of three confocal planes. Scale bar represents 2 μm.

(F) MBP-Mia1p copellets with taxol-stabilized MTs. MBP and MBP-Mia1p were incubated in the absence (−) or presence (+) of MTs and centrifuged through a glycerol cushion. Pellet and supernatant were separated by SDS-PAGE and stained with Coomassie blue.

(G) Dissociation constant K_D of the MBP-Mia1 complex with MTs, as determined by MT spin-down assays. Nonlinear regression was performed on the standard binding equation for a macromolecule containing n equivalent noninteracting ligand-binding sites.

were unaffected. Thus, the dynamics of individual MTs were not discernibly altered in *mia1Δ151-300* cells.

Wild-type MT bundles exhibited persistent overlap regions (Figure 2E; [4, 8, 16]). Interestingly, *mia1Δ151-300* cells showed prominent defects in bundle stability. First, bundles often broke under compression from MT polymerization at cell tips (Figures 2F and 2I). MTs could fuse and rebundle (0.035 events min^{-1} versus 0.033 events min^{-1} in wild-type and *mia1Δ151-300* cells, respectively; n = 32 cells). Second, overlaps were often lost when one of the bundled MTs depolymerized (Figures 2G and 2I). Third, nascent MTs frequently unbundled from underlying "mother" MTs (Figures 2H and 2I). When newly nucleated MTs (appearing away from preexisting overlaps) did remain bundled, their sliding velocities were erratic (see kymographs of Mal3p-GFP-labeled plus ends in Figure 2J; Movies S1 and S2), even though MT growth rates did not diverge from the wild-type (Figure S3G). In contrast to the wild-type, in which MT velocities decayed uniformly while approaching the bundle midzone, MTs often sped up in *mia1Δ151-300* cells. We observed similar behavior with GFP-α-tubulin as a marker (Figures S4A and S4B). Because we did not detect any instances of MT treadmilling or minus-end instability (Figure S4C), we attributed the differences in velocity trajectories solely to MT sliding. We concluded that bundles—but not individual MTs—are unstable when Mia1p does not crosslink MTs.

To understand the reason for bundle instability, we explored the dynamics of the lateral crosslinker Ase1p [9, 17]. MT overlaps labeled by Ase1p-GFP were less persistent in *mia1Δ151-300* cells than in the wild-type (Figure 3A). Nascent Ase1p-GFP entities marking sliding MTs frequently disappeared in *mia1Δ151-300* cells but persisted in the wild-type (survival probability 0.52 versus 0.80, n = 50 entities; Figure 3B). Congruously, less Ase1p associated with MTs in *mia1Δ151-300* cells than in the wild-type (15.2% ± 0.3% versus 21.5% ± 0.5%, n > 120 cells; Figure 3C). As expected, the integrated fluorescence intensity of Ase1p-GFP (proportional to crosslinker number), but not mean fluorescence intensity (proportional to crosslinker density), strongly correlated with MT length ($r = 0.74$, $p < 0.01$, n = 31; see also [8]). Interestingly, crosslinker density was lower in *mia1Δ151-300* cells than in the wild-type ($p < 0.01$, Figure 3D). This lower density could be attributed to an increase in Ase1p off rate. Indeed, fluorescence recovery after photobleaching (FRAP) showed that Ase1p was relatively stable on MT overlaps in wild-type cells (Figures 3E and 3F), consistent with previous reports [8]. In *mia1Δ151-300* cells, Ase1p-GFP exhibited a decrease in mean recovery half-time and a correspondingly higher off rate (Figures 3E and 3F). We concluded that Ase1p is highly dynamic when Mia1p does not bundle MTs.

An increase in Ase1p off rate in the absence of Mia1p crosslinking might indicate that they function synergistically. Indeed, *ase1Δ mia1Δ151-300* cells showed virtually no medial MT overlaps—a stronger phenotype than in single deletions (Figure 3G), frequent spindle abnormalities (Figures S5A and S5B), and compromised growth (Figure S5C). Loss of both Ase1p and Mia1p resulted in cell death (Figure S5D, 70 tetrads). Concordantly, an artificially elevated Ase1p dosage partially suppressed the medial bundling defect in *mia1Δ151-300* cells (Figures S5E–S5G). Given that, at its physiological concentration, most Ase1p is cytosolic (Figure 3C), this rescue indicates that the Ase1p-MT complex has a high dissociation constant. However, because the rescue is partial, it appears that Mia1p appreciably contributes to MT bundling and functions nonredundantly with Ase1p. In light of the physiological concentration of Mia1p (0.24 μM), the measured dissociation constant K_D of the Mia1p-MT complex (0.88 μM) suggests direct bundling by Mia1p as a viable mechanism.

In order to test the plausibility of a mechanism in which lack of Mia1p results in increased dissociation of Ase1p, we modeled—notwithstanding the strong medial bundling phenotype of *mia1Δ151-300* cells—the sliding behavior of nascent bundles. We simulated the stochastic binding kinetics of Ase1p bridging a "daughter" MT sliding along a "mother" in the presence or absence of length-independent Mia1p crosslinking (Figure 4A; Supplemental Experimental Procedures). Ase1p dimers were treated as finitely extensible springs that distributed equally along MT overlaps and dissociated under shear. Crosslinker accumulation retarded the motor Klp2p, stalling the motion of the "daughter." We measured Ase1p density experimentally (Figure 3D) and estimated the contribution of Mia1p to crosslinking from the Ase1p overexpression experiment. The model had two free parameters: the on rate of Ase1p crosslinkers bound to both "mother" and "daughter" and an exponential term determining the dependence of Ase1p off rate on shear force. We performed Monte Carlo simulations [18] of Ase1p binding, dissociation, and shear (Figure 4B). For a broad parameter space, these predicted a higher Ase1p off rate in the absence of Mia1p, especially for short MTs (Figure 4C), consistent with FRAP experiments (Figures 3E and 3F). When the free parameters were tuned to best fit experimentally determined values, we found that Ase1p off rate comprised a large force-dependent component. Furthermore, the simulations suggested that loading of Ase1p onto MTs is the rate-limiting step in array formation. We concluded that the presence of the length-independent, terminal crosslinker Mia1p, in addition to Ase1p, could ensure stable bundling and prevent the loss of Ase1p from MT arrays under shear.

Two aspects of Mia1p-mediated crosslinking are intriguing. First, although Mia1p localization is skewed toward the flanks of overlaps in living cells, it laterally crosslinks MTs in vitro. Interestingly, when overexpressed, Mia1p spreads indiscriminately along the length of MT bundles (Figure S6A), reminiscent of its localization in vitro. In conditions in which the concentration of the protein is limiting, its binding to MTs is likely affected by other factors. For instance, Mia1p does not localize to MT overlaps in the absence of the γ-tubulin accessory factor Mto1p [16, 19–21] (Figure S6B), suggesting that its localization and function in living cells could be modified by this, and possibly other, proteins. Second, Mia1p exhibits an approximately 2-fold preference for antiparallel crosslinking

(H) Recombinant Mia1p bundles rhodamine-labeled MTs. MTs were visualized 5 min after protein addition. Inset: MTs incubated with bovine serum albumin (BSA) as control. Scale bar represents 5 μm.

(I) Transmission electron microscope images of MT bundles. Scale bar represents 0.2 μm.

(J) Recombinant Mia1p crosslinks MTs into both parallel and antiparallel bundles. Dual-color-labeled MTs (magenta minus ends and green plus ends) were visualized 5 min after adding Mia1p. Illustrations below each image show the polarity of bundled MTs.

(K) His_6Mia1p-GFP localizes to MT overlaps in vitro. Rhodamine-labeled MTs visualized 1 min after protein addition.

(L) Fluorescence intensity profiles of His_6-Mia1p-GFP and rhodamine-labeled MTs in the boxed area in (K) show that Mia1p localizes to MT overlaps.

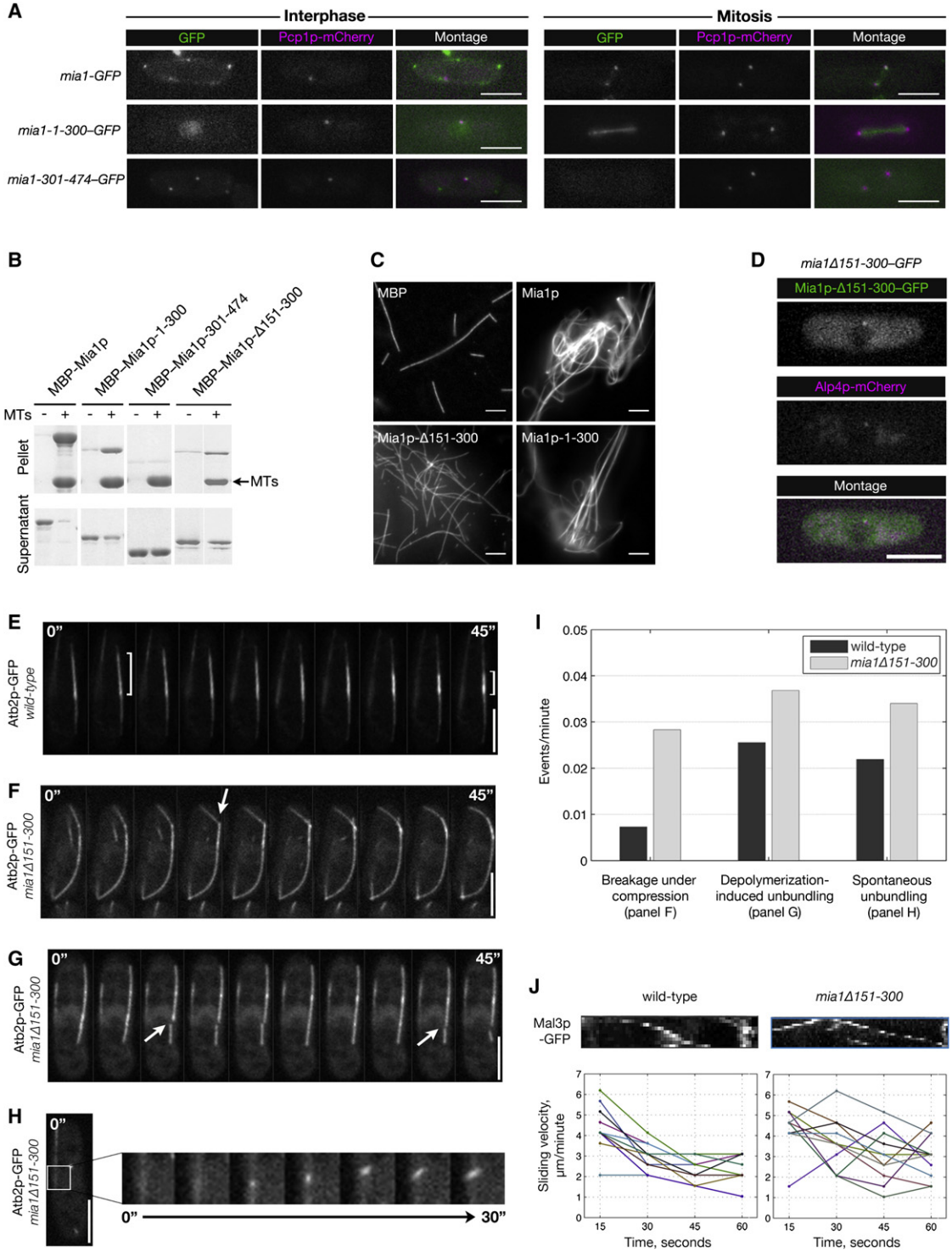

Figure 2. Mia1p-Δ151-300 Is a Truncation Mutant Specifically Deficient in Microtubule Bundling

(A) Single maximum-intensity reconstructions of live cells expressing Mia1p, Mia1p-1-300, and Mia1p-301-474 truncation mutants tagged with GFP. Spindle pole bodies (SPBs) are marked by Pcp1p-mCherry.

(B) MBP-Mia1p-1-300 and MBP-Mia1-Δ151-300 cosediment with MTs in a spin-down assay, whereas MBP-Mia1p-301-474 does not.

(C) Rhodamine-labeled MTs after a 10 min incubation with recombinant Mia1p and truncation constructs. Note that Mia1p-Δ151-300 does not bundle MTs. MBP served as a negative control.

(D) Mia1p-Δ151-300-GFP localizes to the SPB marked by Alp4p-mCherry but is depleted from MTs.

(E) Single-plane time-lapse sequence (5 s interval) of MT arrays in wild-type cells. Brackets show focusing of the MT overlap region over time.

(F) Single-plane time-lapse sequence (5 s interval) of MT arrays in *mia1Δ151-300* cells. Arrow shows bundle breakage under compression.

(G) Single-plane time-lapse sequence (5 s interval) of MT arrays in *mia1Δ151-300* cells. Arrows show separate events of MT overlap loss due to depolymerization of a bundled MT.

in vitro, which is reminiscent of the behavior of Ase1p or a kinesin-5 motor [8, 22]. Possible explanations could involve Mia1p oligomerization, interaction with other MT-binding proteins, and posttranslational modifications.

Our observation that MT arrays were destabilized in the absence of Mia1p bundling was surprising because it was not obvious how the loss of a terminal bundler could destabilize extensive overlaps bridged by Ase1p. One possible explanation invokes force sensitivity in crosslinker off rate. Because the motor moves its lengthening MT cargo with a constant force, the shear on individual Ase1p crosslinkers would be greatest when their number is small. In the absence of terminal crosslinking to dampen such forces, the dissociation of Ase1p from MTs could be conceivably amplified. Such shear-induced dissociation of Ase1p would account for the increase in average Ase1p off rate in *mia1Δ151-300* cells (Figures 3E and 3F). Indeed, our simulations predicted a large force-dependent component in Ase1p off rate, relative to its intrinsic turnover. Fluctuations in the number of lateral crosslinkers would translate into variable load on Klp2p, and it is tempting to proffer this as an explanation for erratic MT sliding in *mia1Δ151-300* cells (Figure 2J). Cooperative interactions between neighboring Ase1p crosslinkers [23] could amplify binding and dissociation events, contributing to such behavior. Thus, Mia1p may stabilize MT arrays by (1) complementing Ase1p braking force acting on kinesin and (2) dampening fluctuations in Ase1p density along MT overlaps. A variation of such a mechanism that keeps Ase1p off rate in check may also stabilize medial MT overlaps that experience compression forces from MT polymerization at cell tips. Linear MT bundles are formed in many differentiated cells [1, 24], and our findings could, in principle, extend to such systems.

Experimental Procedures

Schizosaccharomyces pombe Strains and Constructs

S. pombe strains used in this study and their genotypes are listed in Table S1. Y. Hiraoka (Kobe Research Laboratories) kindly provided the pREP1-GFP-α-tubulin construct. The *nmt1-GFP*-mal3 and *mia1-3GFP* strains were gifts from D. Brunner (European Molecular Biology Laboratory, Heidelberg, Germany) and M. Sato (Tokyo University). Homologous recombination was used to tag endogenous proteins with green fluorescent protein (GFP) or mCherry at C termini. Plasmids were constructed via standard molecular biology techniques. MBP and chaperone plasmids were kind gifts of A. Didovik (Harvard University).

Image Acquisition and Analysis

Epifluorescence still images were typically acquired with a mercury lamp as an illumination source with appropriate sets of filters on a Zeiss Axiovert 200M microscope equipped with a CoolSNAP camera (Photometrics) and Uniblitz shutter driver (Photonics) under the control of MetaMorph software (Universal Imaging). Images were deconvolved via adaptive 3D blind deconvolution with appropriate acquisition settings in AutoQuant (Media Cybernetics).

Time-lapse fluorescence microscopy images, as well as single-time-point z stacks for quantification, were generated on a Zeiss Axiovert 200M microscope equipped with an UltraView RS-3 confocal system: CSU21 confocal optical scanner, 12-bit digital cooled Hamamatsu Orca-ER camera (Opelco), and krypton-argon triple line laser illumination source (488, 568, and 647 nm) under the control of UltraView software (PerkinElmer Inc.). We typically acquired a single plane image every 5 s (time-lapse) or z stacks of nine sections through whole cells, spaced at 0.6 μm (single time point). Imaging was performed on *S. pombe* cells placed in sealed growth chambers containing 2% agarose yeast extract with supplements (YES) medium. Images were processed with Adobe Photoshop and in-house macros developed for ImageJ (National Institutes of Health).

Kymographs of Mal3p-GFP (Figure 2J) were constructed with 4-pixel-wide lines with MetaMorph software (Molecular Devices) and were used to measure sliding velocities by manual tracking of bright pixels.

We determined the amount of Ase1p-GFP associated with MTs (Figure 3C) by threshold selecting areas from normalized images of single cells with a value (0.48) that was visually judged to cover the brightest areas of Ase1p-GFP overlap while maintaining acceptable bleed-through to the cytosolic fluorescence and was comparable in both wild-type and *mia1Δ151-300* cells. The mean value of the thresholded selection was then divided by total cell fluorescence to determine the MT-associated fraction of Ase1p-GFP per cell.

Ase1p-GFP intensity profiles (Figures S5E and S5G) were created from confocal image stacks (nine sections, 0.6 μm spacing). Sum-intensity projections of the z stacks were background corrected by subtracting from each pixel the mean intensity of wild-type cells imaged in the same field. Individual cells in the field were subsequently rotated to orient their long axis horizontally, their fluorescence intensity was normalized, and ImageJ was used to create an intensity profile along the central long axis of a bounding rectangle. We normalized profiles of pooled data by dividing the intensity values by the maximum intensity value in the sample. Mean profiles were then created by plotting the mean intensity values of points in 20 bins along the cell axis.

Fluorescence Recovery after Photobleaching Assay and Data Analysis

A Zeiss LSM 510 scanning confocal microscope equipped with a 63×/1.4 NA Plan Apo objective lens was used to photobleach circular areas of ~1 μm diameter on single bundles in Ase1p-GFP-expressing *S. pombe* cells (Figure 3E). Cells were visualized with a long-pass 505 nm filter. Following initial bleaching with an argon-krypton laser (10 mW, 488 nm) at 100% power, images were acquired at 5 s intervals. Time-lapse average intensity measurements, $I_F(t)$, of the bleached region were taken with ImageJ software, corrected for background bleaching by dividing by fluorescence of the entire imaging field, and normalized as $\hat{I}_F(t) = [I_F(t) - I_F(0)]/[I_F(-\Delta t) - I_F(0)]$, where $I_F(-\Delta t)$ represents fluorescence intensity before bleaching and $I_F(0)$ is the first intensity measurement following bleaching. $\hat{I}_F(t)$ data were fit to a single-exponential curve $\hat{I}_F(t) = I_{EQ}(1 - \exp(-k_{OFF}t))$ by a nonlinear least-squares fit (with the MATLAB fminsearch routine) with parameters I_{EQ} and k_{OFF}, which assumes dominance of Ase1p binding over diffusion [25]. Recovery half-times were subsequently calculated as $\log_e(2)/k_{OFF}$ and averaged over 22 experiments (Figure 3F).

Supplemental Data

Supplemental data include Supplemental Experimental Procedures, one table, six figures, and two movies and can be found online at http://www.cell.com/current-biology/supplemental/S0960-9822(09)01823-5.

Acknowledgments

We are grateful to A. Didovik and M. Sato for sharing reagents and to E. Makeyev, M. Thattai, J.S. Wang, G. Wright, P. Rørth, and F. Uhlmann for discussions and critical reading of the manuscript. This work has been supported by the Temasek Life Sciences Laboratory and the Singapore Millennium Foundation.

Received: March 27, 2009
Revised: September 28, 2009
Accepted: September 29, 2009
Published online: October 29, 2009

(H) Left: an image of MTs in *mia1Δ151-300* cells at the start of the time-lapse sequence. Right: zoomed-in single-plane time-lapse sequence (5 s interval) of the boxed region, showing spontaneous unbundling of a newly nucleated MT from the underlying "mother" MT.
(I) Frequencies of MT unbundling events observed in *mia1Δ151-300* (light gray bars) versus wild-type (dark gray bars) cells.
(J) Top: kymographs of Mal3p-GFP-labeled MT plus ends sliding in a minus-end-directed fashion in wild-type and *mia1Δ151-300* cells. Bottom: velocity-versus-time plots showing individual trajectories of sliding MTs. Note the disordered acceleration in *mia1Δ151-300* cells (right) and an overall slow decay in the wild-type (left).
All scale bars represent 5 μm.

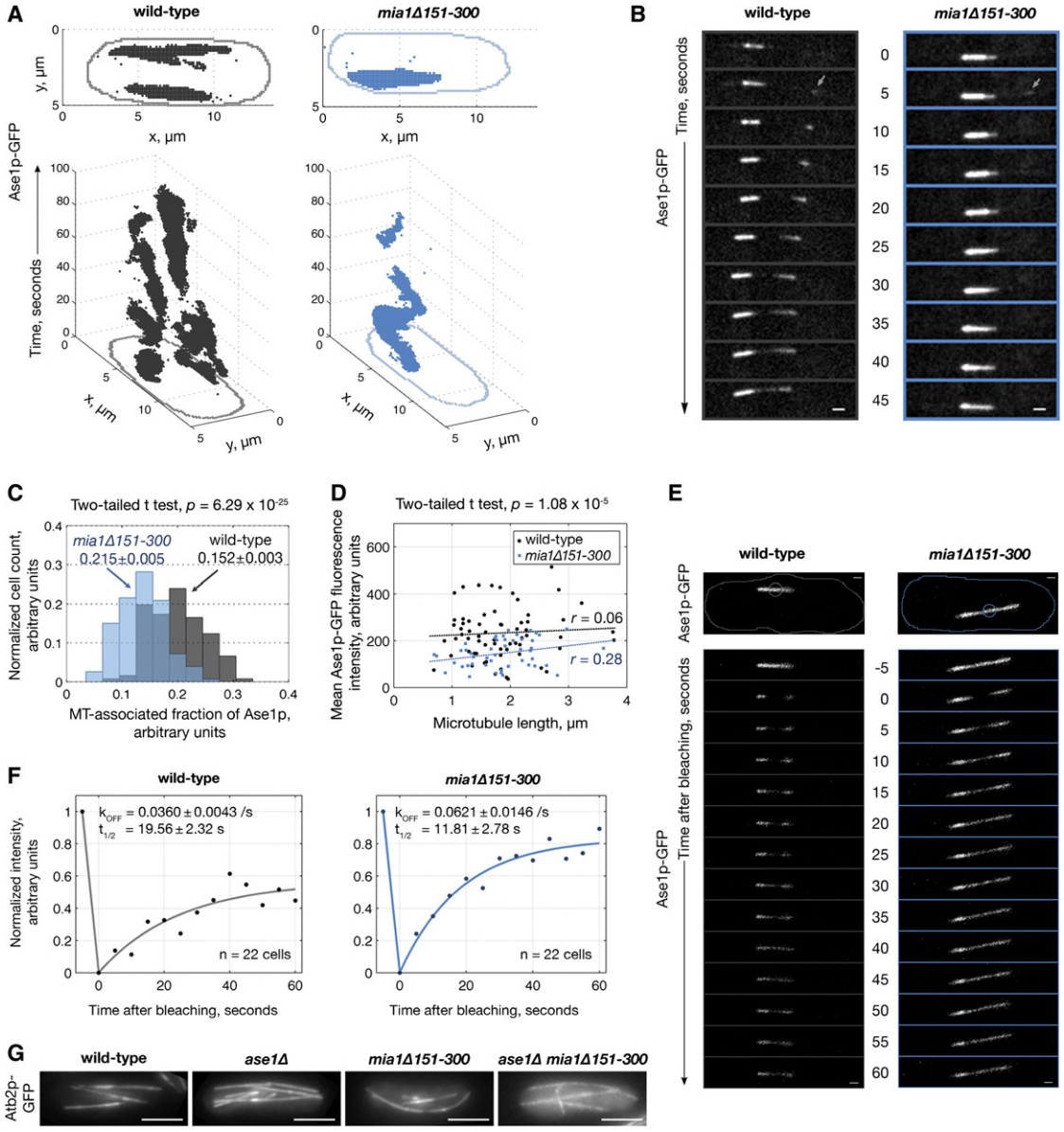

Figure 3. Regions of Microtubule Overlap Defined by Ase1p Are Less Stable in *mia1Δ151-300* Than in Wild-Type Cells

(A) Top: sum-intensity projections of thresholded Ase1p-GFP fluorescence intensity imaged at 5 s intervals for 100 s. Bottom: time evolution of overlaps.

(B) Time-lapse sequence of nascent Ase1p-GFP entities (indicated by arrows in frame 2), imaged at 5 s intervals, in wild-type (left) and *mia1Δ151-300* (right) cells. In *mia1Δ151-300* cells, the entities (nascent MT bundles) often do not survive long enough to be incorporated into an existing region of overlap. Scale bars represent 1 μm.

(C) Fraction of cellular Ase1p associated with MTs in wild-type (gray) and *mia1Δ151-300* (blue) cells. Numbers are indicated as mean ± standard error of the mean (SEM). Two-tailed two-sample t test, $p = 6.29 \times 10^{-23}$.

(D) Mean Ase1p-GFP fluorescence intensity along single pairs of MTs does not strongly correlate with overlap length in wild-type and *mia1Δ151-300* cells. Note that the density of Ase1p molecules is lower in *mia1Δ151-300* cells (two-tailed two-sample t test, $p = 1.08 \times 10^{-5}$).

(E) Top: fluorescence recovery after photobleaching (FRAP) in wild-type and *mia1Δ151-300* cells, with cell boundaries and circular photobleached areas of ~1 μm diameter outline. Bottom: time-lapse images at 5 s intervals of Ase1p-GFP recovery in wild-type and *mia1Δ151-300* cells (bundles bleached in second frame). Scale bars represent 1 μm.

(F) Representative fluorescence recovery curves with Ase1p off rates (k) and recovery half-times (τ) indicated as mean ± SEM.

(G) *ase1Δ mia1Δ151-300* cells show no medial MT overlap regions, unlike *ase1Δ* or *mia1Δ151-300* cells; MTs are marked by GFP-α-tubulin. Scale bars represent 5 μm.

References

1. Bartolini, F., and Gundersen, G.G. (2006). Generation of noncentrosomal microtubule arrays. J. Cell Sci. *119*, 4155–4163.
2. Dammermann, A., Desai, A., and Oegema, K. (2003). The minus end in sight. Curr. Biol. *13*, R614–R624.
3. Yu, W., Cook, C., Sauter, C., Kuriyama, R., Kaplan, P.L., and Baas, P.W. (2000). Depletion of a microtubule-associated motor protein induces the loss of dendritic identity. J. Neurosci. *20*, 5782–5791.
4. Carazo-Salas, R.E., Antony, C., and Nurse, P. (2005). The kinesin Klp2 mediates polarization of interphase microtubules in fission yeast. Science *309*, 297–300.

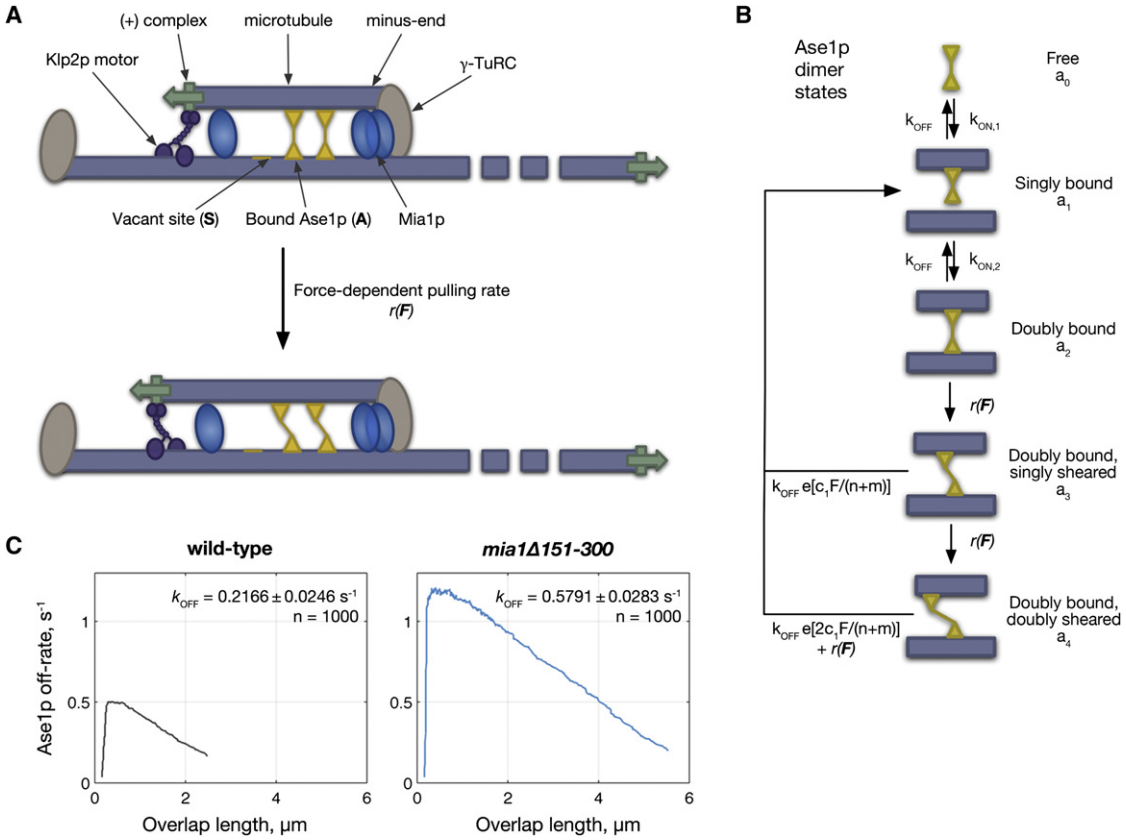

Figure 4. Model of Linear Microtubule Array Formation

(A) Model of nascent MT bundle formation: an MT is nucleated by the γ-tubulin ring complex (γ-TuRC) along a preexisting MT and is pulled toward the minus end of the "mother" MT by Klp2p, which exerts a load-dependent force. As the "daughter" MT grows, the nascent bundle is stabilized by crosslinkers: Ase1p along the length of the MT, and Mia1p in a length-independent manner.

(B) Ase1p dimer states in the computer model: free dimers bind to MTs as vacant binding sites become available, first to a single MT, and then to both MTs in a nascent bundle. Doubly bound Ase1p dimers exert force as they are sheared by the motion of Klp2p in 8 nm step sizes and detach after two steps. The off rates of sheared Ase1p dimers are exponentially dependent on the sum of forces in the system.

(C) Predicted off rates of Ase1p as a function of "daughter" MT length in wild-type and *mia1Δ151-300* cells from a sample stochastic simulation of Ase1p kinetics. Note the higher off rate for short MTs in *mia1Δ151-300* cells.

5. Hoog, J.L., Schwartz, C., Noon, A.T., O'Toole, E.T., Mastronarde, D.N., McIntosh, J.R., and Antony, C. (2007). Organization of interphase microtubules in fission yeast analyzed by electron tomography. Dev. Cell *12*, 349–361.

6. Sawin, K.E., and Tran, P.T. (2006). Cytoplasmic microtubule organization in fission yeast. Yeast *23*, 1001–1014.

7. Daga, R.R., Lee, K.G., Bratman, S., Salas-Pino, S., and Chang, F. (2006). Self-organization of microtubule bundles in anucleate fission yeast cells. Nat. Cell Biol. *8*, 1108–1113.

8. Janson, M.E., Loughlin, R., Loiodice, I., Fu, C., Brunner, D., Nedelec, F.J., and Tran, P.T. (2007). Crosslinkers and motors organize dynamic microtubules to form stable bipolar arrays in fission yeast. Cell *128*, 357–368.

9. Loiodice, I., Staub, J., Setty, T.G., Nguyen, N.P., Paoletti, A., and Tran, P.T. (2005). Ase1p organizes antiparallel microtubule arrays during interphase and mitosis in fission yeast. Mol. Biol. Cell *16*, 1756–1768.

10. Peset, I., and Vernos, I. (2008). The TACC proteins: TACC-ling microtubule dynamics and centrosome function. Trends Cell Biol. *18*, 379–388.

11. Zheng, L., Schwartz, C., Wee, L., and Oliferenko, S. (2006). The fission yeast transforming acidic coiled coil-related protein Mia1p/Alp7p is required for formation and maintenance of persistent microtubule-organizing centers at the nuclear envelope. Mol. Biol. Cell *17*, 2212–2222.

12. Wolf, E., Kim, P.S., and Berger, B. (1997). MultiCoil: A program for predicting two- and three-stranded coiled coils. Protein Sci. *6*, 1179–1189.

13. Ling, Y.C., Vjestica, A., and Oliferenko, S. (2009). Nucleocytoplasmic shuttling of the TACC protein Mia1p/Alp7p is required for remodeling of microtubule arrays during the cell cycle. PLoS ONE *4*, e6255.

14. Demeter, J., Morphew, M., and Sazer, S. (1995). A mutation in the RCC1-related protein pim1 results in nuclear envelope fragmentation in fission yeast. Proc. Natl. Acad. Sci. USA *92*, 1436–1440.

15. Sato, M., Vardy, L., Angel Garcia, M., Koonrugsa, N., and Toda, T. (2004). Interdependency of fission yeast Alp14/TOG and coiled coil protein Alp7 in microtubule localization and bipolar spindle formation. Mol. Biol. Cell *15*, 1609–1622.

16. Janson, M.E., Setty, T.G., Paoletti, A., and Tran, P.T. (2005). Efficient formation of bipolar microtubule bundles requires microtubule-bound gamma-tubulin complexes. J. Cell Biol. *169*, 297–308.

17. Yamashita, A., Sato, M., Fujita, A., Yamamoto, M., and Toda, T. (2005). The roles of fission yeast ase1 in mitotic cell division, meiotic nuclear oscillation, and cytokinesis checkpoint signaling. Mol. Biol. Cell *16*, 1378–1395.

18. Gillespie, D.T. (1976). A general method for numerically simulating the stochastic time evolution of coupled chemical reactions. J. Comput. Phys. *22*, 403–434.

19. Sawin, K.E., Lourenco, P.C., and Snaith, H.A. (2004). Microtubule nucleation at non-spindle pole body microtubule-organizing centers requires fission yeast centrosomin-related protein mod20p. Curr. Biol. *14*, 763–775.

20. Venkatram, S., Tasto, J.J., Feoktistova, A., Jennings, J.L., Link, A.J., and Gould, K.L. (2004). Identification and characterization of two novel

proteins affecting fission yeast gamma-tubulin complex function. Mol. Biol. Cell *15*, 2287–2301.
21. Zimmerman, S., and Chang, F. (2005). Effects of {gamma}-tubulin complex proteins on microtubule nucleation and catastrophe in fission yeast. Mol. Biol. Cell *16*, 2719–2733.
22. van den Wildenberg, S.M., Tao, L., Kapitein, L.C., Schmidt, C.F., Scholey, J.M., and Peterman, E.J. (2008). The homotetrameric kinesin-5 KLP61F preferentially crosslinks microtubules into antiparallel orientations. Curr. Biol. *18*, 1860–1864.
23. Kapitein, L.C., Janson, M.E., van den Wildenberg, S.M., Hoogenraad, C.C., Schmidt, C.F., and Peterman, E.J. (2008). Microtubule-driven multimerization recruits ase1p onto overlapping microtubules. Curr. Biol. *18*, 1713–1717.
24. Baas, P.W., Vidya Nadar, C., and Myers, K.A. (2006). Axonal transport of microtubules: The long and short of it. Traffic *7*, 490–498.
25. Sprague, B.L., Pego, R.L., Stavreva, D.A., and McNally, J.G. (2004). Analysis of binding reactions by fluorescence recovery after photobleaching. Biophys. J. *86*, 3473–3495.